hydrology

MDPI

Article

Analysis of Soil Infiltration Characteristics and Their Influencing Factors Under Different Vegetation Based on a PLS-SEM Model

Xuemin Tang [1,2,3], Yutong Peng [1], Jianli Zhang [1,*], Dandan Li [4,5], Yang Cao [2,3], Weiquan Zhao [2,3] and Yunjie Wu [1]

[1] College of Eco-Environmental Engineering, Guizhou Minzu University, Guiyang 550025, China; tangminmin2024@outlook.com (X.T.); pyt992472923@163.com (Y.P.); wyjzxcvbn@163.com (Y.W.)
[2] Guizhou Institute of Mountain Resource, Guizhou Academy of Sciences, Guiyang 550001, China; cy200612@163.com (Y.C.); zwq82@163.com (W.Z.)
[3] Pingtang Karst Peak-Cluster Depression Ecosystem Observation and Research Station of Guizhou Province, Qiannan Buyei and Miao Autonomous Prefecture 558300, China
[4] School of Karst Science, Guizhou Normal University, Guiyang 550025, China; lddsharing@126.com
[5] School of Geography and Environment Science, Guizhou Normal University, Guiyang 550025, China
* Correspondence: 201901037@gzmu.edu.cn

Abstract

Urban rocky desertification areas are characterized by shallow soils, rock–soil mosaics, and strong human disturbance, so infiltration processes may differ from those in homogeneous soils. However, interactions among multiple controlling factors remain insufficiently quantified. This study compared soil infiltration under artificially restored vegetation (planted grassland (PG) and planted woodland (PW)), and natural secondary vegetation (secondary grassland (SG) and secondary woodland (SW)). Saturated hydraulic conductivity (*Ks*) and falling-head duration (*T*) were measured using falling-head tests on undisturbed soil columns. Soil physical properties were then integrated with partial least squares structural equation modeling (PLS-SEM) to assess the effects of rocky desertification, soil aggregates, and porosity. Soil bulk density was significantly lower under artificially restored vegetation, whereas capillary porosity, non-capillary porosity, and water-holding capacity were significantly higher ($p < 0.05$). Infiltration performance followed PW > PG > SW > SG. PLS-SEM indicated that rocky desertification (−0.78), porosity (0.51), and aggregates (−0.03) jointly regulated infiltration, with non-capillary porosity as the dominant positive factor. Higher infiltration in artificially restored plots was mainly associated with improved pore structure. These findings support vegetation configuration and soil–water management in urban rocky desertification areas.

Keywords: vegetation restoration; soil infiltration characteristics; structural equations; ecological restoration

Check for updates

Academic Editor: Rusu Teodor

Received: 14 June 2026
Revised: 18 July 2026
Accepted: 19 July 2026
Published: 22 July 2026

Copyright: © 2026 by the authors. Licensee MDPI, Basel, Switzerland. This article is an open access article distributed under the terms and conditions of the Creative Commons Attribution (CC BY) license.

1. Introduction

Karst regions are typically ecologically fragile areas characterized by severe soil erosion, with significant vulnerability, hidden risks, and complexity [1,2]. Rapid urbanization has triggered urban ecological degradation, characterized by exposed bedrock, soil erosion, and an imbalance in the hydrological cycle [3]. Extensive impermeable surfaces severely impede the infiltration of surface water, disrupting the balance of the urban hydrological cycle [4]. This region receives heavy rainfall that is unevenly distributed throughout the year; intense or prolonged rainfall often exceeds the city's drainage capacity, resulting in

severe flooding [5,6]. Frequent extreme precipitation events and unsustainable human activities have accelerated rocky desertification in this region, resulting in a distinctive vegetation–soil–rock structure [7]. Within this structure, surface and subsurface runoff converge, producing rapid and pronounced hydrological responses and exhibiting typical yet complex dynamics of soil and water loss [8].

Hydrological processes are closely linked to vegetation cover and ecosystem productivity [9], and vegetation restoration is an effective strategy for reducing soil erosion and protecting the ecological environment [10]. Both natural succession and afforestation are important approaches for restoring ecologically fragile areas. Compared with natural vegetation, artificial vegetation restoration is generally more effective in improving soil properties and structure, while more complex vegetation structures are more favorable for enhancing soil infiltration performance [11]. Reseeding native plant species in degraded areas can rapidly accelerate vegetation establishment and increase biomass [12]. The resulting increases in vegetation cover and height may reduce soil erosion, enhance water infiltration, and improve soil water retention [13]. During precipitation events, vegetation regulates soil water infiltration through multiple pathways [14]. Canopy interception reduces the direct impact of raindrops on the soil surface, thereby mitigating splash erosion, while stems channel precipitation toward the roots through stemflow. Root penetration and litter decomposition jointly alter soil physicochemical properties, pore structure, and water-holding capacity, thereby affecting the redistribution of precipitation [15,16]. As vegetation restoration progresses, soil structure gradually improves, porosity increases, and soil infiltration capacity improves [17]. There are significant differences in the effects of different vegetation types and restoration methods on soil infiltration [18,19]. Studies have shown that various types of vegetation restoration (such as natural secondary forests and planted ecological forests) have significantly different effects on deep soil water [20]. There are also significant differences in soil infiltration among different vegetation restoration models [21]. Soil infiltration in planted forests is superior to that of natural grasslands, planted grasslands, and shrublands, and the higher infiltration rates help improve water use efficiency and reduce soil erosion [11].

Soil infiltration is a hydrological property of soil primarily determined by its texture, structure, and moisture content; it plays a significant role in soil water redistribution and soil and water conservation [22,23]. Karst landscapes are characterized by a spatially mosaic distribution of soil and bedrock due to carbonate rocks, and exposed bedrock plays a significant role in influencing soil water infiltration processes. The unique "rock–soil" interface alters the physical structure of the soil and the pathways of water movement, thereby affecting soil infiltration properties [24]. In rocky desertification areas, porosity and clay content are the primary factors affecting soil infiltration [25]. Soil aggregates influence soil pore distribution through their particle-size distribution and stability; a well-connected, large-pore structure reduces resistance to soil water movement and promotes effective infiltration [26,27]. In addition, characteristics such as gravel content and particle size have varying degrees of influence on water infiltration in soil [28]. Wu et al. found that as the gravel content and particle size increase, the permeability of soil water decreases, while the water-holding capacity of gravelly soil increases [29]. Soil water-holding characteristics, such as capillary water-holding capacity, can further regulate the water available to vegetation and the process of evapotranspiration [30].

Previous studies have largely focused on infiltration processes under a single vegetation type, a single soil physical factor, or relatively homogeneous soil conditions. In contrast, urban karst rocky desertification areas are characterized by shallow soils, rock–soil mosaics, high rock fragment content, and intense anthropogenic disturbance, and their underlying surface heterogeneity may alter soil pore connectivity and water transport

pathways. Therefore, comparisons of infiltration among vegetation types alone are insufficient to explain the interactions among rocky desertification intensity, soil texture, pore structure, and aggregate characteristics. Under two vegetation restoration modes, this study examined planted grassland, planted woodland, natural secondary grassland, and natural secondary woodland by combining falling-head permeability tests on undisturbed soil columns, measurements of soil physical properties, and PLS-SEM path analysis. The objectives were to (1) compare soil infiltration characteristics among ecological restoration modes; (2) identify the principal factors controlling soil infiltration; and (3) quantify the direct and indirect pathways through which rocky desertification intensity, pore structure, and aggregate characteristics affect infiltration performance. The findings provide a basis for vegetation configuration and integrated soil–water management in urban karst areas.

2. Materials and Methods

2.1. Study Area

The study was conducted at the experimental site of Guizhou Minzu University in Guizhou Province, China (106°37′13″ E, 26°22′43″ N). The region has a typical humid subtropical monsoon climate, with concurrent warm and rainy seasons, a mean annual temperature of 15.6 °C, and a mean annual precipitation of 1385 mm. Interannual variation in precipitation is relatively small, and more than 80% of the annual rainfall occurs from May to September [31]. Restoration modes were classified according to vegetation origin and the degree of human intervention as artificially restored vegetation and natural secondary vegetation. The former refers to vegetation established through artificial planting or sowing and subsequently maintained, including planted grassland (PG) and planted woodland (PW); the latter refers to vegetation that regenerates naturally without intensive human intervention, including natural secondary grassland (SG) and natural secondary woodland (SW) [32]. The four types of plots in the study area, classified by restoration pattern and land use type, are shown in Table 1. The rock fragment content (RC, %) for each soil layer under different vegetation cover is shown in Table 2.

Table 1. Basic information on substrate plots under different vegetation types.

Plot Number	Restoration Mode	Land Use Type	Vegetation Structure	Dominant Plant Species
PG	Artificially restored vegetation	Grassland	Shrub, Grass	*Pyracantha fortuneana (Maxim.) H. L. Li*, *Lolium perenne L.*
PW	Artificially restored vegetation	Woodland	Tree, Shrub, Grass	*Cinnamomum camphora* (L.) *J. Presl*, *Ginkgo biloba* L., *Cycas revoluta Thunb.*, *Cynodon dactylon* (L.) *Persoon*
SG	Natural secondary vegetation	Grassland	Shrub, Grass	*Coriaria nepalensis Wall.*, *Arthraxon hispidus* (*Thunb.*) *Makino*
SW	Natural secondary woodland	Woodland	Tree, Shrub, Grass	*Koelreuteria paniculata Laxm.*, *Adenanthera microsperma Teijsm.*, *Rubus idaeus* L.

Note: PG and PW are collectively referred to as artificially restored vegetation, while SG and SW are collectively referred to as natural secondary vegetation. The vegetation structure "trees-shrubs-herbs" refers to a three-layer composite structure consisting of trees, shrubs, and herbs; "shrubs-herbs" refers to a two-layer structure consisting of shrubs and herbs.

Table 2. *Rock fragment content* (RC, %) at different soil depths under different vegetation covers.

Plot Number	Restoration Mode	0–10 cm	10–20 cm	20–30 cm	Rock Fragment Content (RC, %)
PG	Artificially restored vegetation	3.08	3.49	4.23	3.60
PW	Artificially restored vegetation	2.86	3.40	3.81	3.36
SG	Natural secondary vegetation	15.53	14.37	15.96	15.29
SW	Natural secondary woodland	7.13	8.32	10.77	8.74

Note: RC = mass of gravel (>2 mm) in the soil sample/total mass of the soil sample × 100%.

2.2. Experimental Design and Investigation

2.2.1. Sample Plot Selection

Four types of plot categories were selected within the study area and classified according to restoration mode into artificially restored vegetation (planted grassland (PG) and planted woodland (PW)) and natural secondary vegetation (secondary grassland (SG) and secondary woodland (SW)). Three 3 m × 3 m replicate plots were established for each category, for a total of 12 survey plots, with a spacing of more than 20 m between plots to ensure independence. The vegetation composition, soil depth, and rock fragment content (*RC*) for each plot are shown in Table 1. Based on the measured *RC* values in the study area and in accordance with the classification standards for rocky desertification in karst regions, the degree of rocky desertification was categorized as no rocky desertification (*RC* = 0–5%), mild rocky desertification (*RC* = 5–10%), and moderate rocky desertification (*RC* = 10–15%).

2.2.2. Sample Collection and Measurement

All soil samples were collected in September 2024. Because karst areas are characterized by shallow soil layers, abundant rock fragments below a depth of 30 cm, and substantial spatial variation in soil thickness, samples were collected from three soil depths (0–10, 10–20, and 20–30 cm) in each plot, with three replicates per depth, yielding a total of 108 ring samples (3 rings × 4 restoration modes × 3 plots × 3 soil depths), which were averaged to 36 independent plot–depth observations for PLS-SEM analysis. The soil samples were passed through a 2 mm sieve to remove rock fragments, plant roots, and other debris, and each sample was divided into two subsamples for determining soil water content and physicochemical properties, respectively.

(1) Soil bulk density (*BD*), total porosity (*TP*), capillary porosity (*CP*), non-capillary porosity (*NCP*), maximum water-holding capacity (ω_{max}), capillary water-holding capacity (ω_{CP}), non-capillary water-holding capacity (ω_{NCP}), and initial soil water content (*SWC*) were determined using the cutting-ring method. The cutting rings were 5.05 cm in diameter and 5 cm in height, with a volume of 100 cm^3. Undisturbed soil cores were collected from each soil depth, transported to the laboratory, and weighed to determine their fresh mass. The soil cores were then placed in flat-bottomed enamel trays, and deionized water was added until it reached the upper surface of the cores. The samples were allowed to absorb water for 12 h until saturation. After saturation, the cores were removed, allowed to drain freely under gravity for 2 h, and weighed; they were subsequently drained for an additional 6 h and weighed again. Finally, the samples were oven-dried at 105 °C for 72 h to constant mass, after which their dry mass was recorded [33].

(2) The particle-size distribution of water-stable aggregates was determined using the wet-sieving method [34]. Air-dried soil samples were gently broken along natural planes of weakness into aggregates approximately 1–2 cm in diameter. A 50 g subsample was placed on the uppermost sieve of a nested sieve set with mesh sizes of 5, 3, 2, 1, 0.5,

and 0.25 mm. After soaking in deionized water for 5 min, the sieve set was vertically oscillated at a frequency of 30 cycles min^{-1} for 5 min. The aggregates retained on each sieve were collected, oven-dried at 60 °C to constant mass, and weighed. The mass percentage of aggregates in each size fraction (R_i) and the mean weight diameter (MWD) were calculated using the following equations [35]:

$$R_i = m_i / 200 \quad (1)$$

$$MWD = \sum_{i=1}^{n} x_i w_i \quad (2)$$

R_i: mass percentage of aggregates of a given particle size (%); m_i: dry mass of aggregates of a given particle size (g); x_i: average diameter of aggregates of a given particle size (mm); w_i: mass percentage of soil aggregates of a given particle size (%).

(3) The rock fragment content (RC, %) was determined gravimetrically. Air-dried soil samples were passed through a 2 mm sieve, and the rock fragments retained on the sieve (>2 mm) were collected and weighed (W_R). The total mass of each soil sample was recorded as W_S. RC was calculated using the following equation:

$$RC = W_R / W_S \quad (3)$$

W_R: mass of stones in soil samples (g); W_S: total mass of soil samples (g).

(4) Saturated hydraulic conductivity (Ks) was determined using the falling-head permeability method. A TST-55 falling-head soil permeameter (Nanjing Soil Instrument Factory, China) was used, consisting mainly of a permeameter cell containing a cutting ring, porous stones, a collar, and upper and lower caps, together with a falling-head tube, water-supply bottle, stopwatch, and thermometer. Undisturbed soil columns with an inner diameter of 5.05 cm and a height of 5.00 cm were installed in the permeameter in their original vertical orientation. The upper and lower surfaces were trimmed level, and filter paper and porous plates were placed at both ends to minimize soil-particle loss and ensure uniform flow. The sidewalls of the soil columns were sealed to prevent preferential flow along the wall. Before measurement, water was supplied slowly from the bottom upward to gradually expel entrapped air. After continuous outflow without visible bubbles was observed at the top, saturation was continued to ensure that the soil columns reached a nearly completely saturated state. During the test, the lower end of each soil column was connected to the falling-head tube, whereas the upper end was maintained as a free-drainage boundary open to atmospheric pressure; water flowed upward under one-dimensional saturated conditions. The falling-head tube was filled to an initial hydraulic head difference, h_1, and a stopwatch was started to record the time, Δt, required for the head to decrease to h_2. Five consecutive falling-head measurements were conducted for each soil column, and the arithmetic mean of the five measurements was taken as the saturated hydraulic conductivity of that column. Three parallel undisturbed soil columns were tested for each plot–soil–depth combination. There were no significant variations in water temperature recorded during the experiment. Saturated hydraulic conductivity at the experimental water temperature was calculated according to Darcy's law as follows [36]:

$$K_s = \frac{aL}{A\Delta t} ln \frac{h_1}{h_2}$$

Ks: saturated hydraulic conductivity ($cm \cdot s^{-1}$); α: cross-sectional area of the falling-head tube (cm^2); A: cross-sectional area of the soil column (cm^2); L: length of the soil

column (5 cm); Δt: elapsed time required for the hydraulic head to decrease from h_1 to h_2 (s); h_1 and h_2: initial and final hydraulic head differences, respectively (cm).

2.3. Statistical Analysis

Replicate measurements obtained within the same plot and soil depth were first averaged, and each plot–soil–depth combination was treated as the statistical unit. Linear mixed-effects models were used to evaluate the effects of vegetation restoration type, soil depth, and their interaction. Normality and homogeneity of variance were assessed using the Shapiro–Wilk and Levene tests. When significant effects were detected, pairwise comparisons of estimated marginal means were performed with a Tukey adjustment. Relationships among variables were evaluated using Pearson correlation analysis according to the data distribution. Statistical significance was set at $p < 0.05$, and data are presented as means ± standard errors. Partial least squares structural equation modeling (PLS-SEM), which is suitable for small samples and non-normally distributed data, was applied in this study [11]. For PLS-SEM, the three ring samples from each plot–depth combination were averaged, yielding 36 independent observations (4 restoration modes × 3 plots × 3 soil depths), using the R package "plspm" (v0.60). The goodness-of-fit (GOF) index and coefficients of determination for endogenous variables (R^2) were used to evaluate the overall predictive performance of the model. Statistical analyses and figure preparation were performed using SPSS 27 and Origin 2024.

3. Results

3.1. Characteristics of Changes in Soil Physical Properties

The analysis of soil texture on the surface beneath different vegetation types is shown in Figure 1. There were significant differences in soil water infiltration and redistribution among soils of different textures. According to the Standard for Geotechnical Testing Methods (GB/T 50123-2019) [37], soil particle sizes are classified as sand and gravel (1–0.05 mm), silt (0.05–0.002 mm), and clay (<0.002 mm). The mass fractions of sand and gravel in the PW, PG, SW, and SG soils were 70.96%, 64.83%, 58.53%, and 53.05%, respectively; silt values were 20.00%, 15.00%, 18.33%, and 18.33%, respectively; and clay values were 9.67%, 20.77%, 23.10%, and 28.00%, respectively.

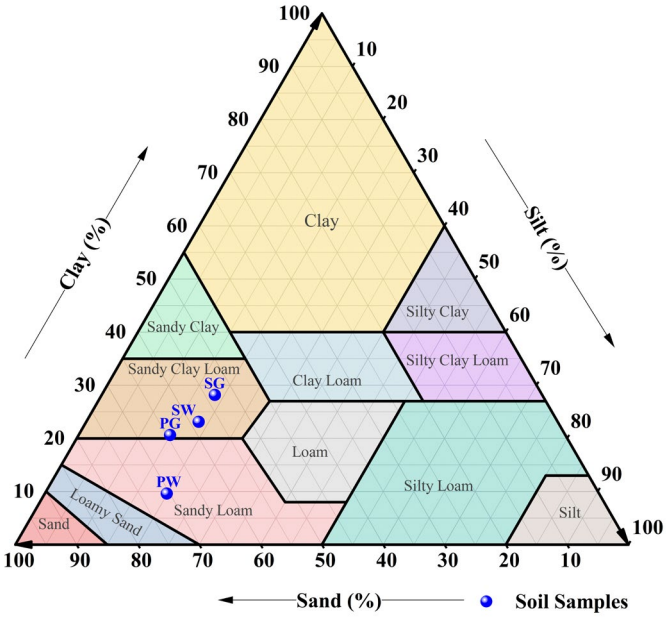


Figure 1. Soil texture type in the study area.

An analysis of the physical properties of the soil subsurface under different vegetation types is shown in Tables 3 and 4. Under different vegetation types, the bulk density (*BD*) of the underlying soil generally increased with depth, with the mean values showing PW (1.08 g·cm^{-3}) < PG (1.13 g·cm^{-3}) < SW (1.25 g·cm^{-3}) < SG (1.33 g·cm^{-3}). Total porosity (TP), capillary porosity (*CP*), non-capillary porosity (*NCP*), maximum water-holding capacity (ω_{max}), and capillary water-holding capacity (ω_{CP}) all decreased with increasing depth. For corresponding vegetation types, the mean soil bulk density (*BD*) values in PW and PG were significantly lower than those in the natural secondary vegetation types, SW and SG, by 13.60% and 15.04%, respectively. Compared with SW, the mean total porosity (TP), capillary porosity (*CP*), non-capillary porosity (*NCP*), maximum water-holding capacity (ω_{max}), and capillary water-holding capacity (ω_{CP}) in PW increased by 4.46%, 3.05%, 32.62%, 11.78%, and 14.82%, respectively; the corresponding increases in PG relative to SG were 4.30%, 2.39%, 33.33%, 2.90%, and 5.56%. Vegetation type was the principal factor influencing *NCP*, while woodland vegetation significantly affected soil *CP* and ω_{max} ($p < 0.05$).

Table 3. Soil bulk density and porosity of substrates under different vegetation types.

Plot Number	Soil Depth (cm)	*BD* g·cm^{-3}	*TP*	*CP*	*NCP*
PW	0–10	1.00 ± 0.04 Cc	51.94 ± 2.99 Aa	47.58 ± 2.20 Aa	4.35 ± 0.79 Aa
	10–20	1.05 ± 0.01 Db	50.61 ± 2.01 Aa	47.77 ± 1.72 Aa	2.84 ± 0.30 Aab
	20–30	1.18 ± 0.01 Ca	48.47 ± 0.37 Aa	46.40 ± 0.30 Aa	2.07 ± 0.07 Aa
PG	0–10	1.03 ± 0.05 Cb	52.07 ± 2.70 Aa	47.73 ± 2.42 Aa	4.33 ± 0.33 Aa
	10–20	1.14 ± 0.01 Cab	49.72 ± 1.70 Aa	46.72 ± 1.45 Aa	3.00 ± 0.26 Ab
	20–30	1.23 ± 0.02 Ca	47.38 ± 0.67 Aa	45.58 ± 0.54 Aa	1.80 ± 0.16 Ac
SW	0–10	1.19 ± 0.01 Bb	48.62 ± 0.53 Aa	45.99 ± 0.51 Aa	2.63 ± 0.03 Ba
	10–20	1.23 ± 0.01 Bb	47.24 ± 1.84 Aa	44.74 ± 1.07 Aa	2.50 ± 0.77 Aa
	20–30	1.32 ± 0.03 Ba	48.70 ± 0.35 Aa	46.82 ± 0.30 Aa	1.87 ± 0.04 Aa
SG	0–10	1.30 ± 0.01 Ab	47.16 ± 0.89 Aa	44.47 ± 0.84 Aa	2.69 ± 0.05 Ba
	10–20	1.31 ± 0.02 Ab	47.44 ± 2.99 Aa	44.65 ± 2.62 Aa	2.79 ± 0.37 Aa
	20–30	1.39 ± 0.01 Aa	48.40 ± 1.11 Aa	47.04 ± 1.39 Aa	1.36 ± 0.43 Ab

Note: *BD* represents soil bulk density, *TP* represents total porosity, *CP* represents capillary porosity, and *NCP* represents non-capillary porosity. Data are presented as mean ± standard error; different uppercase letters indicate significant differences among land use types ($p < 0.05$); different lowercase letters indicate significant differences among vegetation structures ($p < 0.05$).

Table 4. Soil water-holding capacity of the substrate under different vegetation types.

Plot Number	Soil Depth (cm)	ω_{max}	ω_{cp}
PW	0–10	49.74 ± 2.17 Aa	45.74 ± 0.91 Aa
	10–20	49.57 ± 1.77 Aa	43.05 ± 0.36 Aa
	20–30	50.03 ± 2.44 Aa	47.38 ± 1.99 Aa
PG	0–10	50.18 ± 2.92 Aa	49.38 ± 2.37 Aa
	10–20	47.25 ± 0.78 Aa	45.35 ± 0.36 Aa
	20–30	48.21 ± 2.48 Aa	44.86 ± 1.92 Aa
SW	0–10	46.34 ± 1.05 Aa	41.09 ± 1.84 Aa
	10–20	45.09 ± 3.88 Aa	37.21 ± 2.30 Ba
	20–30	42.17 ± 0.32 Aa	40.28 ± 0.46 Aa
SG	0–10	46.12 ± 4.02 Aa	44.13 ± 3.71 Aa
	10–20	49.55 ± 1.74 Aa	44.99 ± 1.58 Aa
	20–30	45.87 ± 5.16 Aa	43.11 ± 4.73 Aa

Note: ω_{max} denotes the maximum water-holding capacity, and ω_{CP} denotes the capillary water-holding capacity. Data are presented as mean ± standard error; different uppercase letters indicate significant differences among land-use types ($p < 0.05$); different lowercase letters indicate significant differences among vegetation structures ($p < 0.05$).

The particle-size distribution characteristics of soil aggregates and the *RC* values of the substrate under different vegetation types are shown in Figure 2A,B. Soil aggregates at different depths were predominantly composed of particles smaller than 0.25 mm; for particles < 0.25 mm, the distribution was SG (25.95%) > PW (23.42%) > SW (23.14%) > PG (19.06%); *MWD* exhibits a trend of first decreasing and then increasing with depth, with average *MWD* values showing SW (2.12 mm) > PW (2.03 mm) > PG (1.89 mm) > SG (1.82 mm); The average *RC* was SG (15.29%) > SW (8.74%) > PW (3.87%) > PG (3.44%). Specifically, the mean *RC* for PW was 1.26 times lower than that for SW ($p < 0.05$), and the mean *RC* for PG was 3.44 times lower than that for SG ($p < 0.01$).

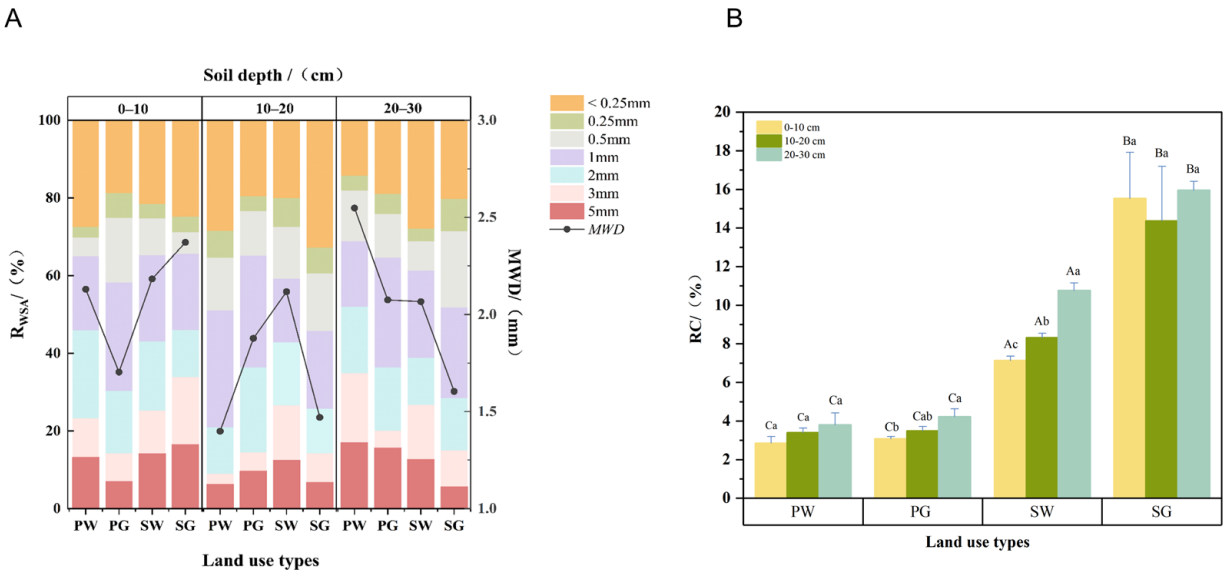


Figure 2. Characteristics of soil aggregates and rock content under different land-use types: (**A**) soil aggregate particle-size distribution and mean weight diameter (*MWD*) at soil depths of 0–10, 10–20, and 20–30 cm; (**B**) rock content (*RC*) at the three soil depths. Different uppercase letters indicate significant differences among land use types ($p < 0.05$); different lowercase letters indicate significant differences among vegetation structures ($p < 0.05$).

Across different vegetation structures, compared with PG, the proportion of $PW_{10–20}$ and $PW_{20–30}$ with $R_{<0.25}$ increased significantly by 46.41% and 46.17%, respectively; furthermore, the $R_{0.50–0.25}$ for $PW_{10–20}$ was significantly higher than that for $PG_{10–20}$ by 73.98%. The *MWD* value for PW was the highest, showing a significant increase of 7.45% compared with that of PG ($p < 0.05$). In natural secondary vegetation, the proportion of $SG_{0–10}$ with $R_{<0.25}$ increased significantly by 15.32% compared to $SW_{0–10}$, and the proportion of $SG_{10–20}$ with $R_{<0.25}$ increased significantly by 63.99% compared to $SW_{10–20}$ ($p < 0.05$).

For different land-use types, there were significant differences between artificially restored vegetation and natural secondary vegetation. The $R_{1.00–0.50}$ value for $PG_{0–10}$ soil was significantly higher than that for $SG_{0–10}$, being 1.77 times greater; the $R_{0.50–0.25}$ value for $PW_{10–20}$ increased by 47.37% compared to that for $SW_{10–20}$ ($p < 0.05$). The $R_{2.00–0.25}$ value for soils under artificially restored vegetation was significantly influenced by vegetation type ($p < 0.05$), and soil depth significantly affected the *MWD* value, with an interaction effect with vegetation type; the *RC* of naturally regenerated vegetation was generally higher than that of artificially restored vegetation and showed an increasing trend with increasing soil depth.

3.2. Soil Infiltration of the Substrate Under Different Vegetation Types

The soil infiltration characteristics of different vegetation subplots are shown in Figure 3. The *SWC* and *Ks* of soils under artificially restored vegetation were both significantly higher than those under natural secondary vegetation, while *T* was significantly shorter ($p < 0.05$). As the soil depth increased, *SWC* and *Ks* showed a decreasing trend, while *T* correspondingly increased; furthermore, the average *SWC*, *Ks*, and *T* across different soil layers were significantly influenced by vegetation type ($p < 0.05$).

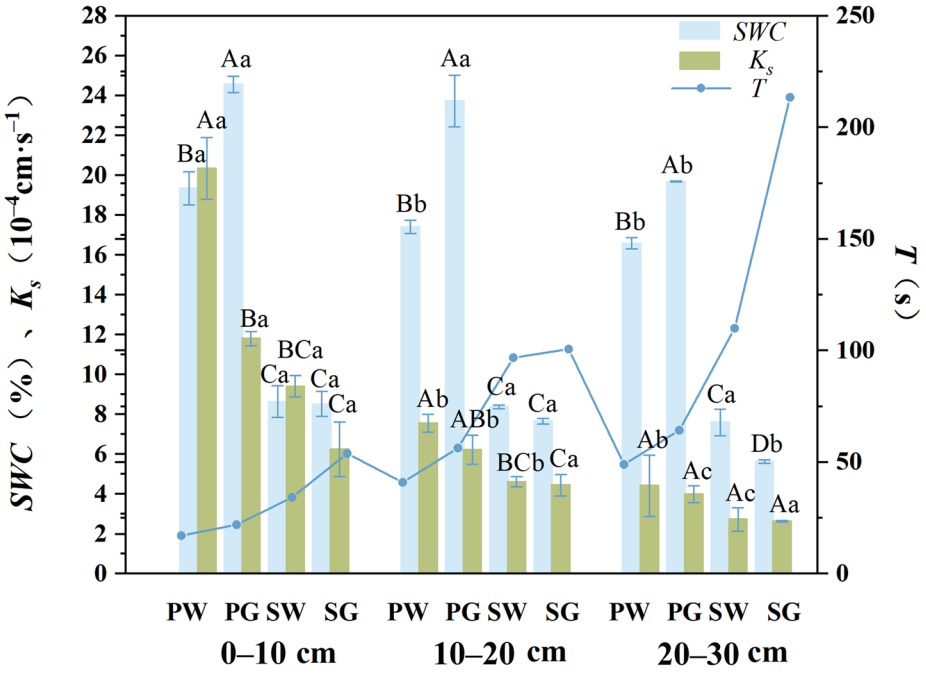


Figure 3. Soil moisture content, average infiltration coefficient, and falling-head duration of various soil layers under different vegetation covers. Different uppercase letters indicate significant differences among land use types ($p < 0.05$); different lowercase letters indicate significant differences among vegetation structures ($p < 0.05$).

Artificial vegetation restoration measures significantly improved soil moisture retention and infiltration capacity. Specifically, the average *SWC* for PW and PG increased by 55.68% and 67.96%, respectively, compared to natural secondary vegetation. The topsoil layer (0–20 cm) of PG showed the greatest increase in *SWC*, reaching 1.19 times and 2.10 times that of SG, respectively. Within the same land-use type, forestland exhibited superior soil infiltration compared to grassland. The *Ks* values for each soil layer in PW increased by 83.10%, 64.89%, and 43.14% compared to PG, respectively; the *Ks* values for $SW_{10–20}$ and $SW_{20–30}$ increased significantly by 38.62% and 35.71%, respectively, compared to $SG_{10–20}$ and $SG_{20–30}$. Under the same vegetation structure, the *Ks* values of each soil layer in PW were 1.29 times, 0.85 times, and 0.15 times those of SW, respectively, while the *Ks* values of $PG_{0–10}$ and $PG_{10–20}$ were 0.25 times and 0.55 times those of $SG_{0–10}$ and $SG_{10–20}$, respectively. The average *T* range for soils in areas with artificially restored vegetation was 17.15–64.29 s, while that for soils in areas with natural vegetation was 34.25–213.51 s; compared with SW and SG, the average *T* for PW and PG decreased by 55.54% and 61.08%, respectively.

3.3. Impact Mechanisms on Soil Infiltration Characteristics in Areas Affected by Rocky Desertification

A correlation analysis was conducted between the physical properties of the soil substrate under different vegetation types and ω_{max}, *Ks*, and *T*, as shown in Figure 4. *RC*

showed a highly significant positive correlation with *BD* and *T* ($p < 0.01$), a significant negative correlation with *NCP* ($p < 0.05$), and a highly significant negative correlation with *Ks* ($p < 0.01$), indicating that as the degree of rocky desertification increases, the combination of soil gravelization and compaction inhibits water infiltration. *BD* was significantly negatively correlated with *CP* and ω_{max} ($p < 0.05$), extremely significantly and negatively correlated with *NCP* and *Ks* ($p < 0.01$), and extremely significantly and positively correlated with *T* ($p < 0.01$). *NCP* was extremely significantly and positively correlated with *Ks* ($p < 0.01$), extremely significantly and negatively correlated with *T* ($p < 0.01$), and significantly positively correlated with ω_{max} ($p < 0.05$).

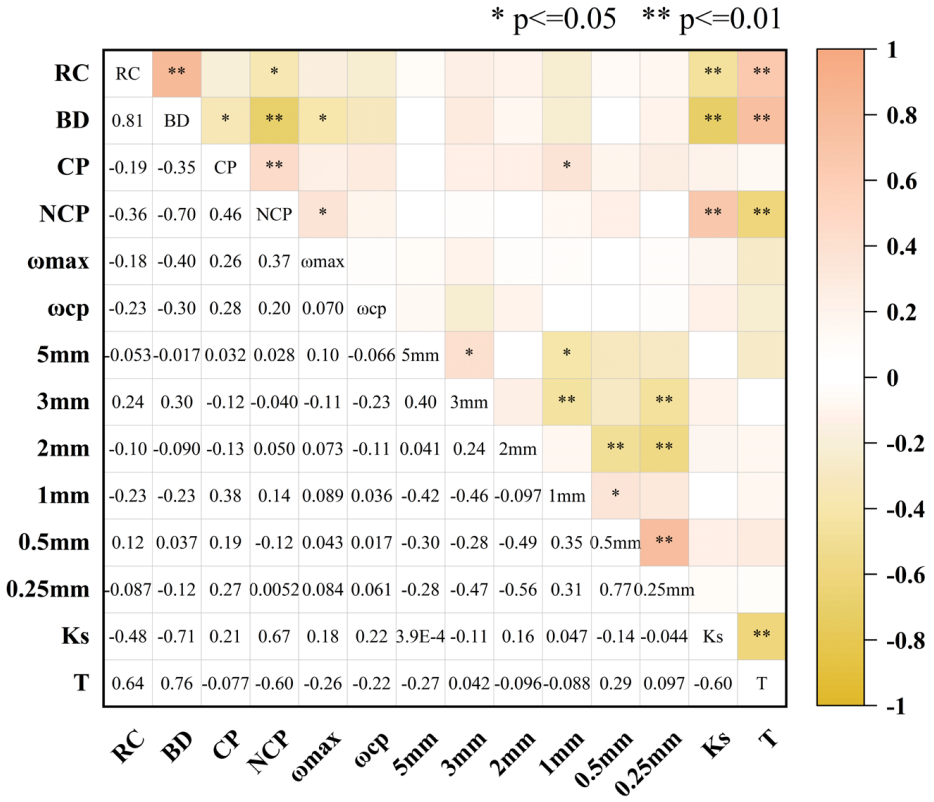


Figure 4. Correlation analysis of underlying surfaces, soil physical properties, and infiltration parameters under different vegetation; 5 mm, 3 mm, 2 mm, 1 mm, 0.5 mm, and 0.25 mm denote the *WSA* particle sizes; * indicates a significant correlation ($p \leq 0.05$), ** indicates a highly significant correlation ($p \leq 0.01$).

To elucidate the direct and indirect pathways through which rocky desertification intensity, soil aggregates, and soil porosity influence soil infiltration properties, partial least squares structural equation modeling (PLS-SEM) was used for path analysis, as shown in Figure 5A,B. The sample size used for model analysis was $n = 36$ (4 restoration modes × 3 plots × 3 soil depths), with each plot–depth combination representing an independent statistical unit. The three ring samples within each plot–depth combination were averaged prior to analysis to avoid pseudoreplication. The model comprised four latent variables; soil porosity and soil infiltration properties were specified as reflective (Mode A) constructs. Soil aggregates were specified as formative (Mode B) because the mass percentages of different aggregate size fractions are compositional variables that collectively form the aggregate characteristics construct. Rocky desertification intensity was specified as a reflective construct represented by *RC* and *BD*. Rocky desertification intensity was reflected by the rock-to-soil ratio (*RC*) and soil bulk density (*BD*); soil aggregates were reflected by the mass percentages of water-stable aggregates in the 5, 3, 2, 1, 0.5, and

0.25 mm size classes ($R_{5\ mm}$–$R_{0.25\ mm}$); soil porosity was reflected by capillary porosity (*CP*) and non-capillary porosity (*NCP*); and soil infiltration properties were reflected by maximum water-holding capacity (ω_{max}), saturated hydraulic conductivity (*Ks*), and falling-head duration (*T*). The measurement model was evaluated in terms of reliability and validity. For the formative construct (soil aggregates), composite reliability and AVE are not applicable; instead, we assessed the significance and relevance of each indicator weight. Based on the outer loadings, composite reliability (CR), and average variance extracted (AVE) of each latent variable, the standardized loadings of the observed variables ranged from 0.61 to 0.94 and were all significant ($p < 0.05$), with *NCP* (0.94) and *T* (−0.88) showing the highest loadings. The CR values of the latent variables ranged from 0.78 to 0.92, all exceeding the acceptable threshold of 0.70, while AVE values ranged from 0.52 to 0.73, all exceeding the criterion of 0.50, indicating satisfactory internal consistency and convergent validity. Discriminant validity was assessed using the Fornell-Larcker criterion. The variance inflation factors (VIFs) of all predictor variables ranged from 1.21 to 3.45, well below the threshold of 5.0, indicating no serious multicollinearity in the model.

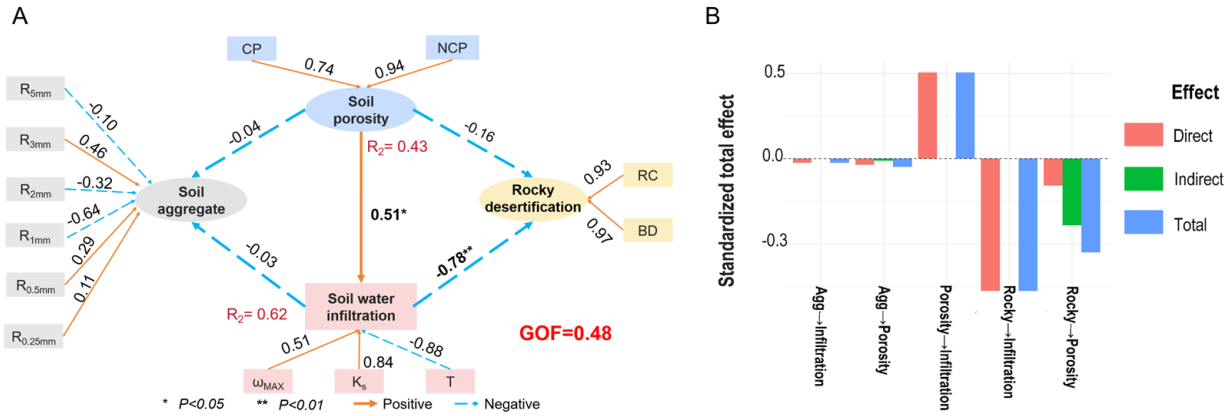


Figure 5. The effects of soil aggregates, rocky desertification degree, and porosity on soil infiltration characteristics were analyzed based on the SEM model. (**A**) Relationships among the latent and observed variables in the structural equation model. Orange solid arrows indicate positive effects, whereas blue dashed arrows indicate negative effects. Values beside the arrows represent standardized path coefficients. * and ** indicate significant effects at $p < 0.05$ and $p < 0.01$, respectively. (**B**) Standardized direct, indirect, and total effects of soil aggregates, rocky desertification, and soil porosity on soil water infiltration. The latent variables include rocky desertification, soil aggregate, soil porosity, and soil water infiltration, while the observed variables include *RC*, *BD*, R_5 mm–$R_{0.25}$ mm, *CP*, *NCP*, ω_{max}, K_s, and *T*.

As shown in Figure 5A, model evaluation was conducted using 500 bootstrap resamples. The goodness-of-fit (GOF) index was 0.48. Rocky desertification intensity had a significant negative direct effect on soil infiltration properties, with a path coefficient of −0.78 ($p < 0.01$). Soil aggregates exerted only a weak direct effect on soil infiltration properties, with a path coefficient of −0.03 ($p > 0.05$). Soil porosity had a significant positive direct effect on soil infiltration properties, with a path coefficient of 0.51 ($p < 0.05$). Rocky desertification intensity had a weak negative direct effect on soil porosity, with a path coefficient of −0.16; its indirect negative effect mediated through soil infiltration properties was −0.40, resulting in a total effect of −0.56. Thus, rocky desertification intensity primarily inhibited the development of soil porosity through an indirect pathway. The model explained 62% and 43% of the variance in soil infiltration properties and soil porosity, respectively (R^2 = 0.62 and 0.43). These results identified rocky desertification intensity, represented primarily by *RC* and *BD*, as a key variable associated with variation in soil infiltration properties. Soil infiltration properties were reflected by *T* (−0.88), *Ks* (0.84), and

ω_{max} (0.51), with their contributions ranked as $T > Ks > \omega_{max}$. Soil porosity was reflected by *NCP* (0.94) and *CP* (0.74), while the direct contribution of $R_{1.00–0.25}$ to the soil aggregate construct was greater than that of $R_{2.00–5.00}$.

4. Discussion

4.1. The Effect of Different Vegetation Covers on Soil Physical Properties

Soil texture, as a key factor influencing water movement, is closely related to physical properties such as soil pore structure and water-holding capacity [38]. This study found that the four combined vegetation types differed not only in vegetation establishment origin and vegetation structure but also significantly in soil particle-size composition ($p < 0.05$). Artificially restored vegetation had higher sand contents and lower clay contents, whereas natural secondary vegetation had relatively higher clay contents. Soil texture can regulate water movement by affecting soil matrix pore size, pore-size distribution, and resistance to water flow. In general, coarse-textured soils have larger matrix pores, whereas higher clay contents may increase flow resistance and reduce the hydraulic conductivity of the soil matrix. These findings are consistent with those reported by Li et al. [39,40]. Sand and clay contents are important variables for predicting near-saturated hydraulic conductivity. In this study, artificially restored vegetation exhibited higher saturated hydraulic conductivity, which was partly associated with its coarser soil texture and thus could not be attributed solely to the effect of vegetation restoration [41]. Water conduction under saturated and near-saturated conditions is governed not only by particle size composition but also by soil structure and the number and connectivity of macropores [42]. Soil porosity can be characterized by total porosity, capillary porosity, and non-capillary porosity. Changes in soil porosity may affect soil water pathways and are closely related to soil infiltration capacity [43]. *NCP* primarily reflects macroporosity, *CP* primarily reflects microporosity, and *BD* primarily reflects total porosity. Research by Zeng et al. indicates that total porosity is the primary factor influencing the steady-state infiltration rate in karst regions [44]. In this study, compared with natural secondary vegetation, artificially restored vegetation exhibited significantly lower soil bulk density (*BD*) and markedly improved pore structure, with significant increases in total porosity (*TP*), capillary porosity (*CP*), and non-capillary porosity (*NCP*) ($p < 0.05$). In particular, *NCP* increased by 32.62–33.33%, substantially enhancing soil water-holding and infiltration capacities. These findings are consistent with those reported by Fu et al. [40]. Changes in soil moisture affect soil infiltration capacity by altering the volume of soil aggregates, which in turn changes soil porosity and connectivity [45]. The $R_{<0.25}$ particle size fraction is a direct factor affecting soil structure, and the distribution of soil pore sizes influences water movement [46]. Root growth, litter inputs, and soil biological activity may enhance soil hydraulic conductivity by improving aggregate structure and promoting the formation of continuous macropores, thereby increasing soil resistance to erosion and improving soil infiltration properties [47]. Previous studies on vegetation restoration have shown that restoration-induced changes in soil porosity, macroporosity, and organic matter can jointly enhance soil infiltration capacity. Under near-saturated conditions, the effects of land use, soil compaction, and management practices on hydraulic conductivity may be comparable in magnitude to those of soil texture. Therefore, the effects of soil texture and vegetation are not mutually exclusive; rather, they may jointly regulate water transmission through two types of flow pathways: matrix pores and structural macropores [43]. In addition, this study found that *RC* affected soil bulk density, pore conditions, and soil water movement. Artificially restored vegetation effectively exhibited lower *RC* values, thereby alleviating the adverse effects of compression at the rock–soil interface on soil pores, prolonging water retention, and enhancing soil infiltration properties in karst areas.

4.2. The Effect of Different Vegetation Covers on Soil Infiltration Characteristics

Differences in vegetation-covered land surfaces affect the vertical distribution of soil water, which is a major factor influencing soil infiltration and evapotranspiration [21]. In this study, artificially restored vegetation areas generally exhibited higher saturated hydraulic conductivity and shorter falling-head durations; however, these differences were more likely associated with root-induced improvements in soil physical properties. Previous studies have shown that a tree–shrub–herb structure can effectively regulate soil pore structure through the distribution of roots at different depths [48]. Roots under a shrub–herb structure can reduce surface soil bulk density (*BD*) and increase soil water-holding capacity and water infiltration. Moreover, a complex vertical vegetation structure can attenuate the negative effects of *BD*, *RC*, and soil depth on soil water content (*SWC*).

Significant differences in *Ks* and *T* were observed among the four underlying-surface types. Artificially restored vegetation exhibited greater infiltration capacity than natural secondary vegetation, and its *T* was significantly shorter than that of natural secondary vegetation ($p < 0.05$). Within the same restoration mode, Ks at all soil depths was significantly higher in PW and SW than in PG and SG, respectively, while *SWC* in the 20–30 cm soil layer was higher in PW and SW than in PG and SG, respectively. These results further indicated a positive association between vegetation restoration and improved soil infiltration performance. Overall, artificially restored vegetation plots exhibited lower *BD*, higher *NCP*, and greater infiltration capacity. Moreover, woodlands with a tree–shrub–herb structure performed better than grasslands with a shrub–herb structure, suggesting that greater complexity of the vertical vegetation structure may favor improvements in soil infiltration properties [49]. From the perspective of soil physical properties, *BD* and *SWC* jointly regulate pore connectivity and the initial soil water status, thereby directly affecting *Ks* and *T*. An increase in *BD* reduces soil pore connectivity, significantly decreases *Ks*, and restricts water infiltration, thereby prolonging *T*. In contrast, higher *SWC* brings the soil column closer to saturation and consequently shortens T. Mean *SWC*, *Ks*, and T across soil depths were significantly affected by vegetation type ($p < 0.05$). Both *SWC* and *Ks* decreased with increasing soil depth, whereas *T* showed the opposite trend. Surface soils exhibited greater water infiltration capacity and storage potential, possibly because of root distribution and organic matter accumulation, whereas increased compaction in deeper soils increased resistance to water movement. In addition, *T* varied widely among the undisturbed soil columns examined in this study, suggesting that *BD* and *SWC* may exhibit threshold effects. *T* may increase markedly when *BD* exceeds a critical value or when *SWC* falls below a certain level. Future studies could further verify these threshold characteristics by conducting gradient experiments using repacked soil columns.

4.3. Analysis of the Mechanisms Affecting Soil Infiltration Properties

Vegetation restoration mode is generally considered a major factor influencing soil infiltration properties because it alters soil physical and chemical characteristics [50]. Using structural equation modeling (SEM), Eldridge et al. analyzed the effects of different vegetation restoration modes on soil water infiltration and found that shrubs exerted an indirect mediating effect on cumulative infiltration by modifying the surface litter layer and its incorporation into the soil [51]. In this study, PLS-SEM was further used to evaluate the effects and relative importance of rocky desertification intensity, soil porosity, and soil aggregates on soil infiltration properties. As a key external driver, rocky desertification intensity exerted the strongest negative direct effect on soil infiltration properties (−0.78) and was primarily represented by the two observed variables *BD* and *RC* [52]. Increasing rocky desertification intensity is often accompanied by reduced soil porosity and increased compaction, which in turn constrain soil water-holding and infiltration capacities. This is

consistent with the high loading of *T* as a major response indicator of rocky desertification intensity (−0.88). The quantity and composition of soil pores exerted a dominant positive influence on infiltration properties. Among the pore-related indicators, *NCP* (0.94) made the greatest contribution to the formation of rapid water-flow pathways and served as a key mediating variable for enhancing overall infiltration capacity. *CP* primarily promotes capillary water retention, whereas *NCP* provides storage space and preferential flow pathways for gravitational water infiltration [40]. Together, they regulate soil water retention and hydraulic conductivity, with the direct effect exceeding the indirect effect. Soil aggregates mainly regulated *Ks*, and the 1.00–0.25 mm aggregate fraction contributed more to structural stability than the larger aggregate fractions. This fraction directly affected soil water-holding and water-transmission capacities and indirectly influenced infiltration by modifying pore-size distribution and pore dimensions, with the direct effect again exceeding the indirect effect. In the integrated representation of infiltration properties, *T* (−0.88), *Ks* (0.84), and ω_{max} (0.51) jointly reflected soil water infiltration characteristics, with their contributions ranked as $T > Ks > \omega_{max}$. This indicates that *Ks* and *T* are the core indicators determining the rate of soil water movement.

This study has several limitations. It was conducted at a single site with limited replication (three plots per vegetation type), based on a space-for-time design without pre-restoration data, and sampling was restricted to one season. Consequently, observed differences between vegetation types may partly reflect initial soil conditions, texture, and rock fragment content rather than vegetation effects alone. Additionally, the observational PLS-SEM analysis does not establish causation [53]. Future studies with long-term monitoring, controlled experiments, or paired-site designs are needed to further separate vegetation effects from legacy effects of site history.

5. Conclusions

(1) Soil physical properties differed significantly among vegetation-covered land surfaces in the urban rocky desertification area. Soil bulk density (*BD*) was lower in artificially restored vegetation plots (PG and PW) than in natural secondary vegetation plots (SG and SW), whereas capillary porosity (*CP*), non-capillary porosity (*NCP*), and water-holding capacity were higher. Soils under artificially restored vegetation were predominantly sandy loam, whereas those under natural secondary vegetation were predominantly clayey. Differences in sand and clay contents between the two restoration types were consistent with the observed differences in infiltration performance.

(2) Soil infiltration performance varied markedly among vegetation-covered land surfaces, following the order PW > PG > SW > SG. Saturated hydraulic conductivity (*Ks*) was higher, and falling-head duration (*T*) was shorter under artificially restored vegetation than under natural secondary vegetation. In addition, woodlands with a tree–shrub–herb structure exhibited better infiltration performance than grasslands, suggesting that greater vertical structural complexity may favor improvements in soil infiltration properties.

(3) The PLS-SEM model further revealed that soil infiltration properties were jointly represented by *T*, *Ks*, and ω_{max}. These variables were jointly regulated by rocky desertification intensity (−0.78), soil porosity (0.51), and soil aggregates (−0.03). Rocky desertification intensity was the principal factor limiting *T*; *NCP* (0.94) was the key mediating variable governing soil water storage and transport pathways; and the 1.00–0.25 mm aggregate fraction contributed more to soil structural stability than the larger aggregate fractions.

https://doi.org/10.3390/hydrology13070197

Author Contributions: Conceptualization, X.T. and Y.W.; methodology, Y.P. and J.Z.; software, Y.P. and J.Z.; validation, D.L., Y.C. and Y.W.; formal analysis, Y.P.; investigation, J.Z. and D.L.; resources, Y.P.; data curation, X.T. and Y.C.; writing—original draft preparation, X.T.; writing—review and editing, X.T. and W.Z.; visualization, X.T. and Y.P.; supervision, Y.C.; project administration, W.Z.; funding acquisition, J.Z. All authors have read and agreed to the published version of the manuscript.

Funding: This research was funded by the Guizhou Provincial Science and Technology Projects (QKHZC [2023] YB151, QKHPTYWZ [2024] 002-02), the Innovation Capacity Building Program of the Guizhou Institute of Mountain Resources (QKSPT [2025] 03), and the Doctoral Research Initiation Project of Guizhou Minzu University (GZMUZK [2024] QD63).

Data Availability Statement: The original contributions presented in this study are included in the article. Further inquiries can be directed to the corresponding author.

Conflicts of Interest: The authors declare no conflicts of interest.

References

1. Zeng, X.; Peng, X.; Liu, T.; Dai, Q.; Chen, X. Runoff generation and erosion processes at the rock–soil interface of outcrops with a concave surface in a rocky desertification area. *CATENA* **2024**, *239*, 107920. [CrossRef]
2. Yuan, J.; Li, R.; Huang, K. Driving factors of the variation of ecosystem service and the trade-off and synergistic relationships in typical karst basin. *Ecol. Indic.* **2022**, *142*, 109253. [CrossRef]
3. Yang, Q.; Chen, J.; Yang, G.; Xie, H.; Li, M.; Sun, J. Dynamic evolution of rocky desertification and vegetation restoration and analysis of driving forces in Southwest Karst Region from 2000 to 2020. *PLoS ONE* **2025**, *20*, e0332644. [CrossRef] [PubMed]
4. Wu, Y.; Luo, Z.; Luo, W.; Ma, T.; Wang, Y. Multiple isotope geochemistry and hydrochemical monitoring of karst water in a rapidly urbanized region. *J. Contam. Hydrol.* **2018**, *218*, 44–58. [CrossRef] [PubMed]
5. Zeng, J.; Yue, F.-J.; Li, S.-L.; Wang, Z.-J.; Wu, Q.; Qin, C.-Q.; Yan, Z.-L. Determining rainwater chemistry to reveal alkaline rain trend in Southwest China: Evidence from a frequent-rainy karst area with extensive agricultural production. *Environ. Pollut.* **2020**, *266*, 115166. [CrossRef] [PubMed]
6. Qin, C.; Li, S.-L.; Waldron, S.; Yue, F.-J.; Wang, Z.-J.; Zhong, J.; Ding, H.; Liu, C.-Q. High-frequency monitoring reveals how hydrochemistry and dissolved carbon respond to rainstorms at a karstic critical zone, Southwestern China. *Sci. Total Environ.* **2020**, *714*, 136833. [CrossRef] [PubMed]
7. Jing, J.; Li, R.; Xiong, L.; Tang, Z. Binary response of runoff generation and erosion processes to karst vegetation-soil-rock structure and its hydrodynamic mechanisms. *J. Hydrol.* **2025**, *647*, 132319. [CrossRef]
8. Berbert-Born, M.; Trajano, E.; Calux, A.; Barbosaa, E.; Ribeiro, L.; Neto, F.; Sánchez, L.; Silva-Sánchez, S.; Neri, A.; Lobo, H. O Carste, um tipo particular de ambiente. In *Guia de Boas Práticas Ambientais em Mineração de Calcário em Áreas Cársticas*; Sociedade Brasileira de Espeleologia: Campinas, Brazil, 2016; pp. 12–27.
9. Cui, Z.; Huang, Z.; Liu, Y.; López-Vicente, M.; Wu, G.-L. Natural compensation mechanism of soil water infiltration through decayed roots in semi-arid vegetation species. *Sci. Total Environ.* **2022**, *819*, 151985. [CrossRef] [PubMed]
10. Wang, D.; Liu, C.; Yang, Y.; Liu, P.; Hu, W.; Song, H.; Miao, C.; Chen, J.; Yang, Z.; Miao, Y. Clipping decreases plant cover, litter mass, and water infiltration rate in soil across six plant community sites in a semiarid grassland. *Sci. Total Environ.* **2023**, *861*, 160692. [CrossRef] [PubMed]
11. Zhang, S.; Zhao, G.; Fan, J.; Yang, M.; Tian, P.; Mu, X.; Geng, R. Variations of soil infiltration in response to vegetation restoration and its influencing factors on the Loess Plateau. *J. Environ. Manag.* **2024**, *372*, 123356. [CrossRef] [PubMed]
12. Duan, C.; Li, X.; Chai, Y.; Xu, W.; Su, L.; Yang, X.; Ma, P. Eco-stoichiometric characteristics of carbon, nitrogen, and phosphorus in degraded alpine meadow under artificial restoration. *Chin. J. Grassl.* **2022**, *44*, 23–32.
13. Tong, Z.; Quan, G.; Wan, L.; He, F.; Li, X. The effect of fertilizers on biomass and biodiversity on a semi-arid grassland of Northern China. *Sustainability* **2019**, *11*, 2854. [CrossRef]
14. Hou, G.; Bi, H.; Huo, Y.; Wei, X.; Zhu, Y.; Wang, X.; Liao, W. Determining the optimal vegetation coverage for controlling soil erosion in Cynodon dactylon grassland in North China. *J. Clean. Prod.* **2020**, *244*, 118771. [CrossRef]
15. Zhang, Y.; Yuan, C.; Chen, N.; Levia, D.F. Rainfall partitioning by vegetation in China: A quantitative synthesis. *J. Hydrol.* **2023**, *617*, 128946. [CrossRef]
16. Yang, Y.; Jing, L.; Li, Q.; Liang, C.; Dong, Q.; Zhao, S.; Chen, Y.; She, D.; Zhang, X.; Wang, L.; et al. Big-sized trees and higher species diversity improve water holding capacities of forests in northeast China. *Sci. Total Environ.* **2023**, *880*, 163263. [CrossRef] [PubMed]
17. Basset, C.; Abou Najm, M.; Ghezzehei, T.; Hao, X.; Daccache, A. How does soil structure affect water infiltration? A meta-data systematic review. *Soil Tillage Res.* **2023**, *226*, 105577. [CrossRef]

18. Qiu, D.; Xu, R.; Wu, C.; Mu, X.; Zhao, G.; Gao, P. Vegetation restoration improves soil hydrological properties by regulating soil physicochemical properties in the Loess Plateau, China. *J. Hydrol.* **2022**, *609*, 127730. [CrossRef]
19. Zhong, Z.; Han, X.; Xu, Y.; Zhang, W.; Fu, S.; Liu, W.; Ren, C.; Yang, G.; Ren, G. Effects of land use change on organic carbon dynamics associated with soil aggregate fractions on the Loess Plateau, China. *Land Degrad. Dev.* **2019**, *30*, 1070–1082. [CrossRef]
20. Li, R.; Wang, Y.; Ji, W.; Liu, W.; Li, Z. Water deficit limits soil organic carbon sequestration under old apple orchards in the loess-covered region. *Agric. Ecosyst. Environ.* **2024**, *359*, 108739. [CrossRef]
21. Zhu, P.; Zhang, G.; Wang, H.; Xing, S. Soil infiltration properties affected by typical plant communities on steep gully slopes on the Loess Plateau of China. *J. Hydrol.* **2020**, *590*, 125535. [CrossRef]
22. Yang, Z.; Huang, X.; She, D. Spatial Distribution Characteristics and Influencing Factors of Soil Saturated Hydraulic Conductivity in the Loess Hilly Region of Northwestern Shanxi. *J. Soil Water Conserv.* **2020**, *34*, 178–184. [CrossRef]
23. Yang, S.; Tian, R.; Wang, H.; Zhang, Y.; Li, H. Specific cation effects on soil water infiltration and soil aggregate stability–Comparison study on variably and permanently charged soils. *Soil Tillage Res.* **2025**, *247*, 106385. [CrossRef]
24. Wang, S.; Yan, Y.; Zhao, Y.; Fu, Z.; Chen, H. Co-evolution among soil thickness, epikarst weathering degree, and runoff characteristics on a subtropical karst hillslope. *J. Hydrol.* **2024**, *628*, 130499. [CrossRef]
25. Li, Y.; Liu, D.; Yang, S.; Chen, H.; Lu, L.; Guo, X.; Yang, Y. Terrace abandonment enhances rather than diminishes hydrological functioning in karst terraces by reshaping soil pore structure. *CATENA* **2026**, *263*, 109749. [CrossRef]
26. Li, Y.; Yu, P.; Shen, L. Changes in soil aggregate stability and aggregate-associated organic carbon during old-field succession in karst valley. *Environ. Monit. Assess.* **2021**, *194*, 15. [CrossRef] [PubMed]
27. Menon, M.; Mawodza, T.; Rabbani, A.; Blaud, A.; Lair, G.J.; Babaei, M.; Kercheva, M.; Rousseva, S.; Banwart, S. Pore system characteristics of soil aggregates and their relevance to aggregate stability. *Geoderma* **2020**, *366*, 114259. [CrossRef]
28. Ma, Y.; Wang, Y.; Zhang, Y.; Zhang, R.; Yuan, C.; Ma, C.; Bai, Y. Effects of gravel on the water infiltration process and hydraulic parameters of stony soil in the eastern foothills of Helan Mountain, China. *Sci. Rep.* **2024**, *14*, 16426. [CrossRef] [PubMed]
29. Wu, X.; Meng, Z.; Dang, X.; Wang, J. Effects of rock fragments on the water infiltration and hydraulic conductivity in the soils of the desert steppes of Inner Mongolia, China. *Soil Water Res.* **2021**, *16*, 151–163. [CrossRef]
30. Sun, J.; Hua, L.; Niu, Y.; Zhang, Z.; Dong, R.; Chu, B.; Sun, W.; Cai, B. Grassland restoration measures influence soil water-holding capacity by altering soil and vegetation properties composition. *Int. Soil Water Conserv. Res.* **2026**, *14*, 100611. [CrossRef]
31. Zi, R.; Han, Z.; Chen, T.; Fang, F.; Fang, Q.; Peng, L.; Qian, X.; Yin, X.; Zhao, L. Quantifying the effects of rock fragments embedding vs. Covering on soil erosion in karst sloping cropland. *CATENA* **2024**, *244*, 108234. [CrossRef]
32. Liu, X.; Feng, T.; Zhang, Y.; Liu, Y.; Wang, P. Vegetation restoration affects soil hydrological processes in typical natural and planted forests on the Loess Plateau. *J. Hydrol.* **2025**, *650*, 132465. [CrossRef]
33. Huang, Z.; Bai, M.; Zhang, Y.; Chen, Y.; Ma, D.; Hu, X. Fine-root morphological traits regulate soil infiltration rate through soil properties in arid shrublands. *Soil Tillage Res.* **2026**, *264*, 107351. [CrossRef]
34. Bai, Q.F.; Wang, Y.Q.; Bao, Y.H.; He, X.B.; Luo, P.; Wei, J. Effects of Vegetation Restoration Patterns on Soil Water-stable Aggregates Composition and Their Stability in the Water Level Fluctuation Zone of the Heilongtan Reservoir. *J. Soil Water Conserv.* **2024**, *38*, 168–176. [CrossRef]
35. Li, J.; Li, J.; Hua, D.; Li, S.; Pang, Z.; Jiang, H. Research on the enhancement material and culture method of soil aggregates composed of feldspathic sandstone and sand. *Sci. Rep.* **2024**, *14*, 16210. [CrossRef] [PubMed]
36. Feng, L.; Chang, D.; Ren, Z.; He, Z.; Cui, K. Research on the relationship between permeability and pore size distribution of soft soil in Zhuhai, China. *KSCE J. Civ. Eng.* **2026**, *30*, 100486. [CrossRef]
37. *GB/T 50123-2019*; Standard for Geotechnical Testing Method. China Planning Press: Beijing, China, 2019.
38. Zeng, Y.; Wang, B.; Yue, R.; Zheng, F.; Gu, W.; Wang, W.; Darboux, F. Impact of initial water content on aggregate stability: A perspective based on soil internal forces. *Geoderma* **2025**, *464*, 117640. [CrossRef]
39. Li, J.; Wang, W.; Guo, M.; Kang, H.; Wang, Z.; Huang, J.; Sun, B.; Wang, K.; Zhang, G.; Bai, Y. Effects of soil texture and gravel content on the infiltration and soil loss of spoil heaps under simulated rainfall. *J. Soils Sediments* **2020**, *20*, 3896–3908. [CrossRef]
40. Fu, T.; Gao, H.; Liang, H.; Liu, J. Controlling factors of soil saturated hydraulic conductivity in Taihang Mountain Region, northern China. *Geoderma Reg.* **2021**, *26*, e00417. [CrossRef]
41. Jian, J.; Shiklomanov, A.; Shuster, W.D.; Stewart, R.D. Predicting near-saturated hydraulic conductivity in urban soils. *J. Hydrol.* **2021**, *595*, 126051. [CrossRef]
42. Beckers, E.; Pichault, M.; Pansak, W.; Degré, A.; Garré, S. Characterization of stony soils' hydraulic conductivity using laboratory and numerical experiments. *Soil* **2016**, *2*, 421–431. [CrossRef]
43. Qiu, D.; Xu, R.; Wu, C.; Mu, X.; Zhao, G.; Gao, P. Effects of vegetation restoration on soil infiltrability and preferential flow in hilly gully areas of the Loess Plateau, China. *CATENA* **2023**, *221*, 106770. [CrossRef]
44. Zeng, J.; He, B.; Li, T.; Chen, Z.; Wu, Y.; Zeng, R. Soil Infiltration Characteristics Under Different Forest and Grass Restoration Models in Karst Trough-valley Region. *J. Soil Water Conserv.* **2019**, *33*, 58–64. [CrossRef]

45. Xiao, J.; Wang, B. Experimental study on the influencing factors of infiltration characteristics of abandoned grassland on slope scale in the loess hilly and gully region. *Adv. Water Sci.* **2020**, *31*, 820–831. [CrossRef]
46. Ming, F.; Chen, L.; Li, D.; Wei, X. Estimation of hydraulic conductivity of saturated frozen soil from the soil freezing characteristic curve. *Sci. Total Environ.* **2020**, *698*, 134132. [CrossRef] [PubMed]
47. Ma, R.-t.; Guo, W.; Hu, F.-N.; Xu, C.-Y.; Liu, G.; Zhao, S.-w.; Zheng, F.-l. Effects of soil internal forces on splash detachment and transport of aggregate fragments in Mollisols of Northeast China. *Eur. J. Soil Sci.* **2022**, *73*, e13273. [CrossRef]
48. Picciafuoco, T.; Morbidelli, R.; Flammini, A.; Saltalippi, C.; Corradini, C.; Strauss, P.; Blöschl, G. On the estimation of spatially representative plot scale saturated hydraulic conductivity in an agricultural setting. *J. Hydrol.* **2019**, *570*, 106–117. [CrossRef]
49. Boluwade, A.; Madramootoo, C.A. Independent principal component analysis for simulation of soil water content and bulk density in a Canadian Watershed. *Int. Soil Water Conserv. Res.* **2016**, *4*, 151–158. [CrossRef]
50. Sun, D.; Yang, H.; Guan, D.; Yang, M.; Wu, J.; Yuan, F.; Jin, C.; Wang, A.; Zhang, Y. The effects of land use change on soil infiltration capacity in China: A meta-analysis. *Sci. Total Environ.* **2018**, *626*, 1394–1401. [CrossRef] [PubMed]
51. Eldridge, D.J.; Beecham, G.; Grace, J.B. Do shrubs reduce the adverse effects of grazing on soil properties? *Ecohydrology* **2015**, *8*, 1503–1513. [CrossRef]
52. Guo, H.; Wang, G.; Sun, S. Effects of Nitrogen Addition on Soil Structure and Water Infiltration of Subalpine Coniferous Forest. *J. Soil Water Conserv.* **2023**, *37*, 238–245. [CrossRef]
53. Ansani, A.; Rinallo, E. PLS-SEM-Power: A Shiny App and R Package for Computing Required Sample Size and Minimum Detectable Effect Size in PLS-SEMs. *arXiv* **2025**, arXiv:2511.14546.

Disclaimer/Publisher's Note: The statements, opinions and data contained in all publications are solely those of the individual author(s) and contributor(s) and not of MDPI and/or the editor(s). MDPI and/or the editor(s) disclaim responsibility for any injury to people or property resulting from any ideas, methods, instructions or products referred to in the content.